

Comparison of Admittance Control Dynamic Models for Transparent Free-Motion Human-Robot Interaction

Christopher K. Bitikofer, Eric T. Wolbrecht *Member, IEEE*, Rene M. Maura, Joel C. Perry *Member, IEEE*

Abstract— This paper presents an experimental comparison of multiple admittance control dynamic models implemented on a five-degree-of-freedom arm exoskeleton. The performance of each model is evaluated for transparency, stability, and impact on point-to-point reaching. Although ideally admittance control would render a completely transparent environment for physical human-robot interaction (pHRI), in practice, there are trade-offs between transparency and stability—both of which can detrimentally impact natural arm movements. Here we test four admittance modes: 1) *Low-Mass*: low inertia with zero damping; 2) *High-Mass*: high inertia with zero damping; 3) *Velocity-Damping*: low inertia with damping; and 4) a novel *Velocity-Error-Damping*: low inertia with damping based on velocity error. A single subject completed two experiments: 1) 20 repetitions of a single reach-and-return, and 2) two repetitions of reach-and-return to 13 different targets. The results suggest that the proposed novel *Velocity-Error-Damping* model improves transparency the most, achieving a 70% average reduction of vibration power vs. *Low-Mass*, while also reducing user effort, with less impact on spatial/temporal accuracy than alternate modes. Results also indicate that different models have unique situational advantages so selecting between them may depend on the goals of the specific task (i.e., assessment, therapy, etc.). Future work should investigate merging approaches or transitioning between them in real-time.

I. INTRODUCTION

A. Background and Motivation

Stroke is a major cause of physical disability, affecting approximately 1.3 million people annually [1]. Arm and hand impairment, which reduces survivor independence, is the most common long-term consequence of stroke [2]. Traditional physical therapy is effective [3] but labor-intensive and expensive to deliver. Aging populations [4] and a limited supply of skilled therapists [5] have inspired the development of robotic solutions to decrease therapy labor requirements, investigate factors that promote recovery, and simultaneously assess and train users [6]–[10]. Research efforts have increasingly sought exoskeleton solutions that can simultaneously assist and train the upper limb and provide features such as gravity support and motion guidance [8], [11]. A growing body of evidence suggests that patient engagement is critical to recovery, with patients benefiting most from higher-intensity/longer-duration therapy and training protocols that continually adapt assistance according to patient performance [12]. Patient engagement can be

This work is supported by NSF Award #1532239 and the Eunice Kennedy Shiver NICHD of the NIH Award #K12HD073945. This paper is solely the responsibility of the authors and does not necessarily represent the official views of the NSF or the NIH

Chris Bitikofer is with the University of Idaho, Moscow, ID 83844-0902 in the Dept. of Mechanical Engineering (biti6400@vandals.uidaho.edu)

Rene Maura is with the University of Idaho, Moscow, ID 83844-0902 in the Dep. of Mechanical Engineering (maur9504@vandals.uidaho.edu)

E. Wolbrecht and J. C. Perry are with the University of Idaho, Moscow, ID 83844-0902 in the Department of Mechanical Engineering (ewolbrec@uidaho.edu and jperry@uidaho.edu).

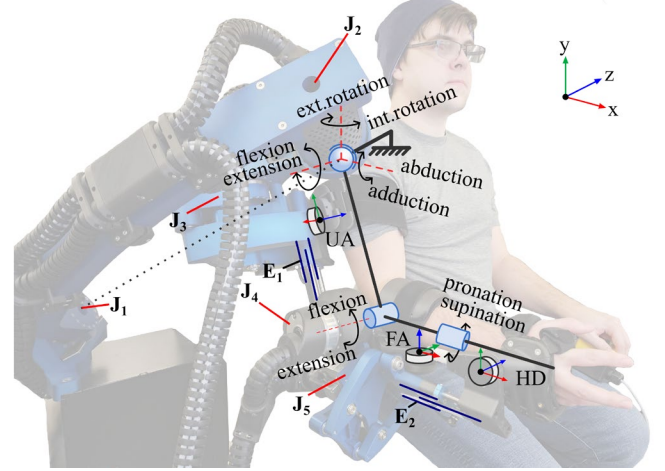


Figure 1. The BLUE SABINO Exoskeleton. The 5-DOF kinematic structure includes three actuators (J_{1-3}) which allow shoulder rotation, one (J_4) for elbow rotation and one (J_5) for forearm pronation/supination. Force sensors are located at the upper arm (UA), forearm (FA), and hand (HD). The structure also includes two arm length adjustments (E_{1-2}).

promoted by assist-as-needed (AAN) approaches that challenge the user by modulating the level of assistance/resistance for training depending on the patient's specific need [13], [14]. Performant AAN requires a highly transparent environment so that the robot does not influence subject-initiated movement when assistance/resistance is not required [15]. However, perfect transparency is not possible for several reasons including difficulty predicting/measuring human-motion intent (HMI) [16], uncertainties in robot dynamics (e.g. friction), and kinematic misalignments between the robot and user [17], [18]. Still, it is important to strive for transparency because the alternative, non-transparent control, can cause the user to change their motor patterns, making assessments of functional capability less accurate [19].

Efforts to improve exoskeleton transparency have included Kalman filtering force signals to tune HMI detection [20], directional-dependent dynamic compensation validated by electromyography activation [15], incorporation of self-aligning features to limit the effects of misalignment [17], and the use of inertial measurement units, series elastic actuators, and virtual mass [21].

Most controllers apply a combination of model-based compensation and state feedback to mask robot dynamics and impose a low-impedance environment [20]–[24]. Controllers usually include heuristically tuned inertial and resistive elements for sufficient disturbance rejection [25], [26]. Capacitive elements are not typically used for free motion but are sometimes employed to guide the user's motion [27], [28]. The appropriate combination of dynamic elements for high transparency is unclear, so we chose to investigate several combinations to compare force interaction performance.

B. Objective

We sought to develop a transparent physical human-robot interaction (pHRI) environment for BLUE SABINO (BiLateral Upper-extremity Exoskeleton for Simultaneous Assessment of Biomechanical and Neuromuscular Output) [29] and thus conducted a preliminary study on the effects of various inertial and damping admittance-model elements on healthy upper-limb motion. Four modes were considered: 1) *Low-Mass*: low inertia with zero damping; 2) *High-Mass*: high inertia with zero damping; 3) *Velocity-Damping*: low inertia with damping; and 4) *Velocity-Error-Damping*: low inertia with damping based on velocity error. *Velocity-Error-Damping* is a novel approach we propose to improve overall transparency while preventing excess vibration disturbance. The proposed force control is simple to implement and can be applied at the joint level negating the need for inverse kinematics or task space parameterization. Also, it requires only force and position sensors. The following sections present BLUE SABINO as an experimental apparatus, the proposed admittance control scheme, and a series of experiments to evaluate the proposed admittance modes.

II. METHODS

A. BLUE SABINO Experimental Apparatus

Experiments are performed using the right-side BLUE SABINO exoskeleton with five actuated joints that allow upper arm movements using shoulder rotation, elbow flexion/extension, and wrist supination/pronation (Figure 1). During experiments, the subject aligns their arm with spatial targets presented by a 3D rendered virtual environment (Figure 2-A). A Speedgoat target computer communicates with system components at 1000 Hz via an EtherCAT network. Interaction forces and torques (F/T) at the human-robot attachments (HRA) are measured by 6-axis sensors located at the upper arm, forearm, and hand (Figure 2-B). The five joints are actuated by Harmonic Drive® brushless motors, which also provide trajectory measurements.

B. Admittance Control

Admittance/impedance controllers are known for their ability to render highly-transparent force environments [30], which is why these paradigms are often applied in exoskeleton control [20],[22]–[24]. Admittance control is implemented on BLUE SABINO to leverage the precision of the joint encoders for inner-loop feedback linearization. The selection of virtual, inertial, and resistive dynamic elements define the force environment rendered to the user [31]. Generally, the lower inertia and resistive parameters are set, the more responsive the control will be to input forces. However, some level of inertia and damping are required to

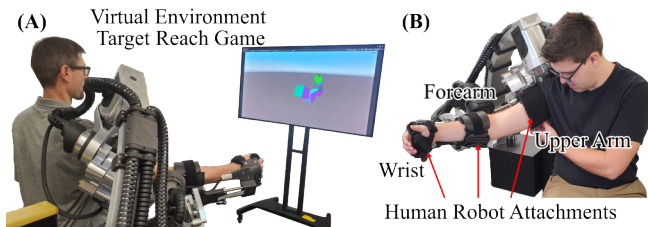


Figure 2. Experimental apparatus. (A) A virtual environment prompts motions and provides spatial and temporal feedback. (B) The 5-DOF version of BLUE SABINO interfaces with the user's upper arm, forearm, and hand. reject disturbances and achieve stable force interaction.

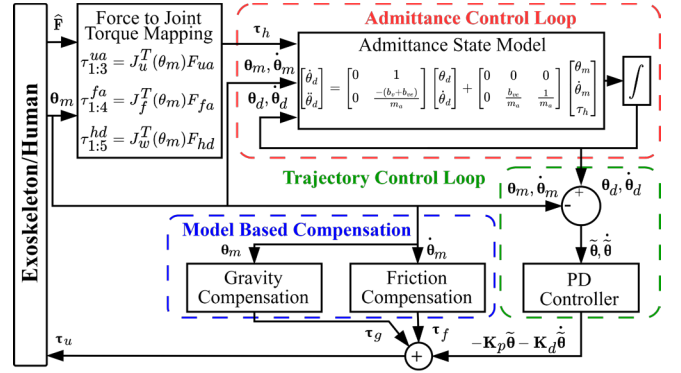


Figure 3. Admittance control scheme for BLUE SABINO 5-DOF.

The joint-level admittance control consists of an outer-loop force controller, referred to as the admittance control loop, paired with an inner-loop trajectory control loop (Figure 3). User applied forces are mapped to joint torques via manipulator Jacobians [32]. The admittance control loop sets the target position and velocity for the trajectory control loop, which computes joint torque commands.

The dynamics of BLUE SABINO can be described as:

$$\mathbf{M}(\boldsymbol{\theta})\ddot{\boldsymbol{\theta}} + \mathbf{C}(\boldsymbol{\theta}, \dot{\boldsymbol{\theta}})\dot{\boldsymbol{\theta}} + \boldsymbol{\tau}_g + \boldsymbol{\tau}_f = \boldsymbol{\tau}_u + \boldsymbol{\tau}_h \quad (1)$$

where \mathbf{M} is the manipulator inertia matrix, \mathbf{C} is the Coriolis matrix, $\boldsymbol{\tau}_f$ is friction torque, $\boldsymbol{\tau}_g$ is gravity torque, $\boldsymbol{\tau}_u$ is the control input vector and $\boldsymbol{\tau}_h$ is the human input torque. Also, $\boldsymbol{\theta}$, $\dot{\boldsymbol{\theta}}$, and $\ddot{\boldsymbol{\theta}}$ are joint position, velocity, and acceleration.

The control input includes model-based compensation for friction and gravity as well as proportional-derivative (PD) tracking of the desired trajectory set by the admittance model. Compared to gravity and friction, inertial torques are relatively small for typical human movement speeds [33], and thus are not included in the control law, similar to [11], [18]. The control law is defined as:

$$\boldsymbol{\tau}_u = -\mathbf{K}_p \tilde{\boldsymbol{\theta}} - \mathbf{K}_d \dot{\tilde{\boldsymbol{\theta}}} + \hat{\boldsymbol{\tau}}_f + \hat{\boldsymbol{\tau}}_g \quad (2)$$

where \mathbf{K}_p and \mathbf{K}_d are positive-definite proportional and derivative term gain matrices respectively. Terms $\tilde{\boldsymbol{\theta}} = \boldsymbol{\theta}_m - \boldsymbol{\theta}_d$ and $\dot{\tilde{\boldsymbol{\theta}}} = \dot{\boldsymbol{\theta}}_m - \dot{\boldsymbol{\theta}}_d$ are joint position and velocity error vectors, respectively, with the m and d subscripts indicating the measured and desired states. Joint friction, $\hat{\boldsymbol{\tau}}_f$, is estimated by experimentally identified sigmoid models that capture coulombic and viscous effects for each motor [34]. Gravity, $\hat{\boldsymbol{\tau}}_g$, is estimated using manipulator kinematics and CAD modeling. The inner-loop PD gains were tuned such that joints accurately track sine wave position inputs spanning the bandwidth of healthy human upper limb motion (0.1 – 3.0 Hz for the shoulder, 0.1 – 5.0 Hz for the elbow and wrist) [33].

C. Design of the Admittance State Model

The joint-level admittance model takes human joint torques (mapped from F/T sensors) and outputs a desired trajectory to the inner-loop controller. The model includes inertia, \mathbf{m}_a , velocity damping, \mathbf{b}_v , and velocity error damping, \mathbf{b}_{ve} . The admittance model has the form:

$$\begin{bmatrix} \dot{\theta}_d \\ \dot{\theta}_d \end{bmatrix} = \begin{bmatrix} 0 & 1 \\ 0 & -(\mathbf{b}_v + \mathbf{b}_{ve}) \end{bmatrix} \begin{bmatrix} \theta_d \\ \dot{\theta}_d \end{bmatrix} + \begin{bmatrix} 0 & 0 & 0 \\ 0 & \frac{\mathbf{b}_{ve}}{\mathbf{m}_a} & \frac{1}{\mathbf{m}_a} \end{bmatrix} \begin{bmatrix} \theta_m \\ \dot{\theta}_m \\ \tau_h \end{bmatrix}. \quad (3)$$

D. Admittance Model Parameter Selection

For the *Low-Mass* mode (LM), a minimum inertia was determined heuristically such that motions can be safely conducted without excessive vibration. The inertia for *High-Mass* (HM) was set to double this minimum. The damping for *Velocity-Damping* (VD) was heuristically tuned to reduce vibration with a resistance feel about halfway between the HM and LM Modes. The novel *Velocity-Error-Damping* mode (VED) was tuned in the same manner. Values used are provided in Table 1.

TABLE 1. ADMITTANCE PARAMETERS

Mode	Abbr.	Term ^a	Unit	Joint				
				J ₁	J ₂	J ₃	J ₄	J ₅
High-Mass	HM	m_a	kg · m	1.2	1.2	0.6	0.6	0.6
Low-Mass	LM	m_a	kg · m	0.6	0.6	0.3	0.1	0.01
Velocity-Damping	VD	m_a	kg · m	0.6	0.6	0.3	0.1	0.01
		b_v	kg · m/s	5	5	3	3	0.5
Velocity-Error-Damping	VED	m_a	kg · m	0.6	0.6	0.3	0.1	0.01
		b_v	kg · m/s	15	15	9	9	1.5
All Modes ^b		K_p	N · m/rad	4000	4000	3000	3000	320
		K_d	N · m · s/rad	200	200	40	40	1

a. Terms not listed for a mode are set to 0.

b. K_p and K_d are set to the same values for all modes.

E. Experiments

Experiments were performed by a single subject (male, age 29) familiar with operating the exoskeleton who provided informed consent to voluntarily participate under University of Idaho IRB 22-093. During experiments, the subject reached for targets presented to them by a 3D virtual environment that shows a rendered version of the user's right arm moving in real time along with the exoskeleton (Figure 4). The target and the hand are considered aligned when the distance and angular orientation errors between the hand and target is less than 10 mm and 10 degrees, respectively. The subject performed two experimental tasks with each pHRI mode: 1) *High Repetition Motion* (HRM), and 2) *Low Repetition Distributed Motions* (LRDM) (Figure 5).

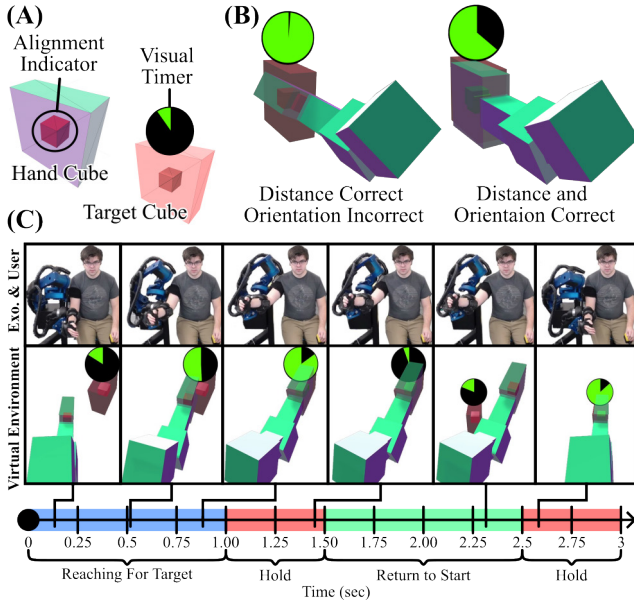


Figure 4. Reaching targets in the virtual environment prompts user motion and provides visual feedback. (A) The hand cube contains a color-changing alignment indicator. Red 3D rectangles denote targets to reach within the time indicated by the green/black circle. (B) The indicator cube switches from red to green once the correct position and orientation are achieved. (C) Still frames from a simultaneous capture of the virtual environment and video recording of the subject performing a single reach and return motion.

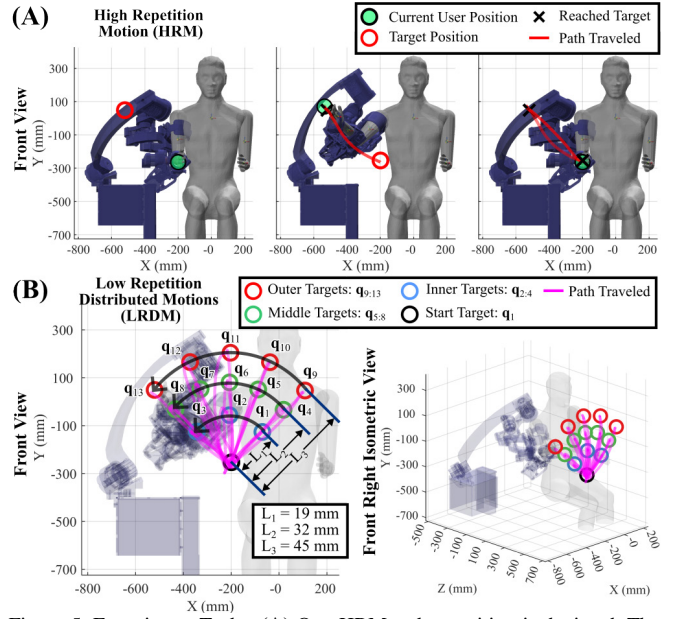


Figure 5. Experiment Tasks. (A) One HRM task repetition is depicted. The user starts from a specified position and is presented a target. They reach for the target, hold still in that position 0.5 sec, then are presented a target at the initial position which they return to complete the repetition. (B) The LRDM task target locations and presentation order are illustrated. Example recorded paths of travel are overlaid in magenta.

The HRM task characterizes the effects of pHRI mode on trajectory consistency and spatial/temporal accuracy using 20 repetitions of a single reach and return motion. The task was conducted 3 times per admittance mode, with the motion tempo set to fast, medium, and slow (0.5 sec, 1 sec, and 2 sec per motion, respectively). The LRDM task examines the effects of the pHRI modes throughout the exoskeleton workspace, using the two repetitions of 13 distinct reach and return motions to targets distributed on three circular shells, such that points on the same shell are equidistant to the start/end motion point.

For each task, the user was prompted by the virtual environment to reach their hand from a home point to a target within a specified time, hold their arm at that location for a period of 0.5 seconds, and then return to the original location (Figure 4-C). Synchronous audio and visuals cued the user to reach the target at the intended time. The subject was allowed ample time to gain familiarity with the device, and rest between tasks to mitigate learning and fatigue effects.

III. RESULTS

A. Vibration/Frequency Content

Frequency analysis was conducted on data from the LRDM experiment. Power spectral density (PSD) content was identified in the human input torque signals (τ_h) which excludes null-space forces and torques. PSD estimates were obtained for each repetition using MATLAB's pwelch function with a 4096-point discrete Fourier transform, a 500-sample hamming window, and an overlap of 50%. Summary statistics including mean, variance, and 95th % confidence intervals were computed over repetitions and motions.

Bandpower was determined by integrating the spectra over three frequency bands, (0-5 Hz, 5-10 Hz and 10-500 Hz), which correspond to human motion, system resonance and the human haptic perception [35]. To highlight differences between modes, results are normalized relative to *Low-Mass* since it exhibited the most vibration (Figure 6).

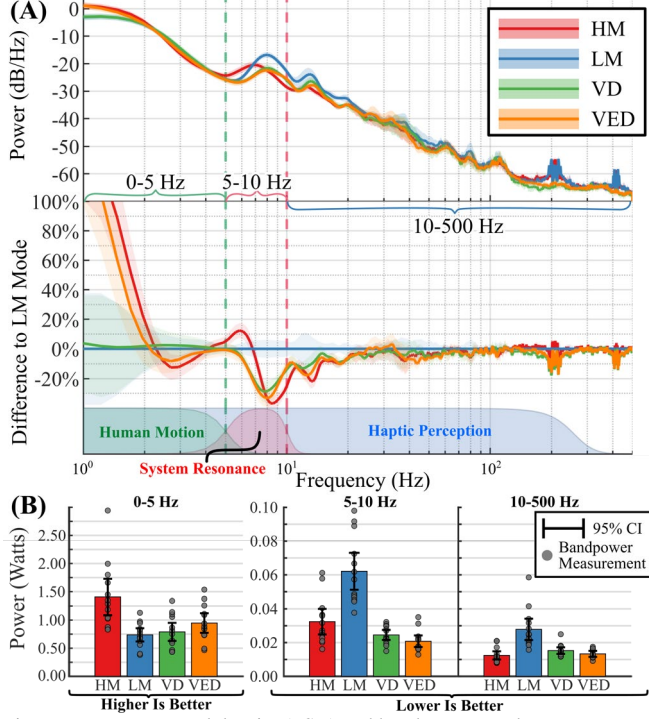


Figure 6. Power spectral density (PSD) and bandpower results.

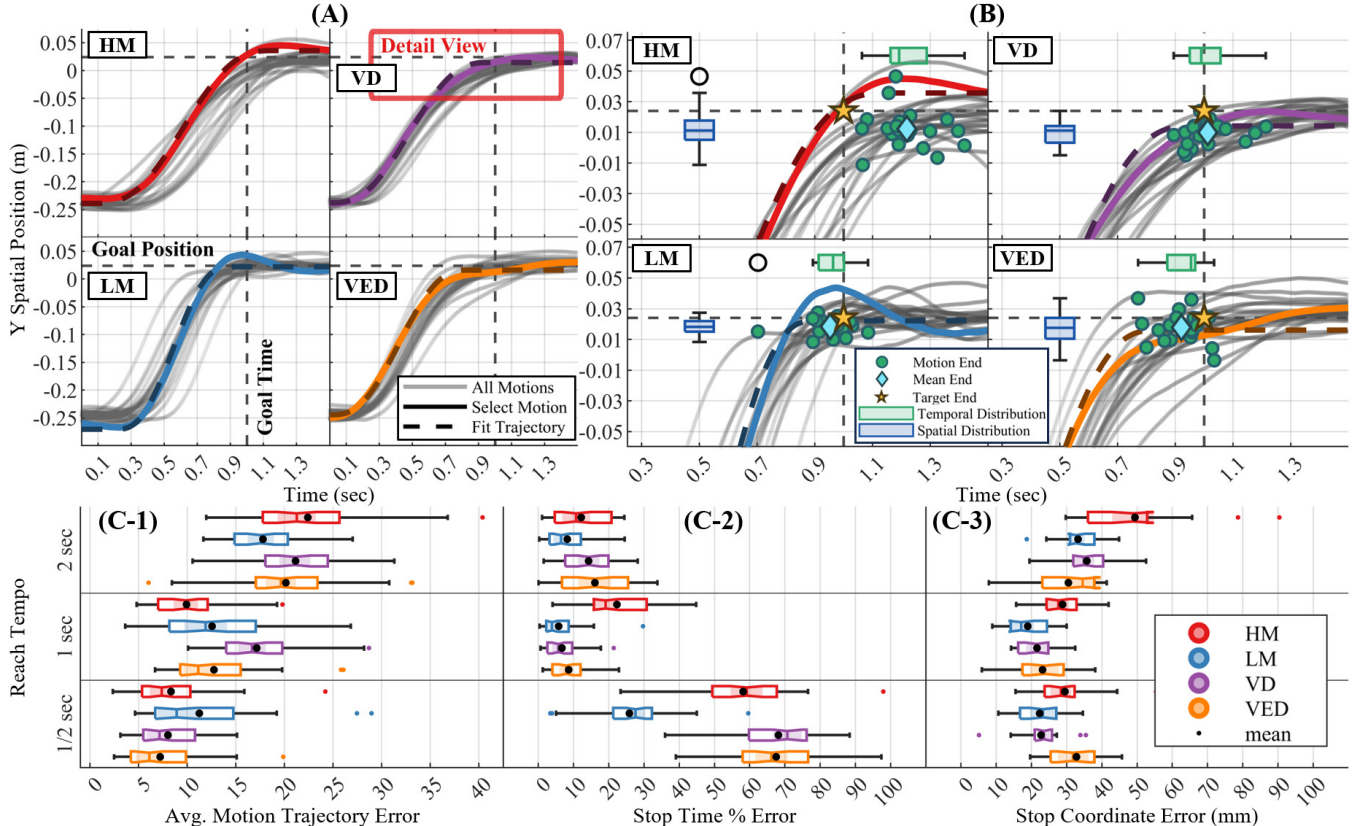


Figure 7. Spatial-temporal analysis results. (A) The 1 sec. HRM reach segments are shown in gray. One example is highlighted in color and shown along with a fit minimum-jerk trajectory. (B) Spatial and temporal error distributions are shown in a detailed view of (A). (C) Distributions of trajectory, arrival time, and position error are shown for each HRM task speed. Low trajectory error indicates natural motion. Low time/coordinate error indicate spatial/temporal accuracy.

B. Spatial Temporal

A minimum-jerk trajectory was fit to the spatial trajectory of each reach segment from the HRM task using a gradient-based solver (MATLAB's `fmincon` function) by determining optimal start/stop times and positions. Trajectory error was computed as the mean difference between the fit and actual trajectories. Stopping time and end reach position errors were computed as the difference between the target arrival time/position and fitting results (Figure 7).

C. Work and Effort

The pHRI mode's work performance is characterized using the HRM motion data to evaluate: 1) mean absolute human work (MAHW), and 2) the proportion of human work output to the total combined human and robot work i.e., the human work percentage (HWP).

MAHW is the cumulative instantaneous human work, calculated as the product of joint velocity measurements and force-sensor mapped joint torques. It is defined as:

$$MAHW = \frac{1}{n} \sum_{i=1}^n \left(\sum_{j=1}^n |\tau_{h(i,j)} \dot{\theta}_{(i,j)}| \right) \quad (4)$$

where n is the number of recorded time samples in each motion segment, i indexes the robot joints, and j indexes sample time. HWP is defined as:

$$HWP = \frac{1}{n} \sum_{i=1}^n \left(\sum_{j=1}^n \left(\frac{|\tau_{h(i,j)} \dot{\theta}_{(i,j)}|}{|\tau_{h(i,j)} \dot{\theta}_{(i,j)}| + |\tau_{r(i,j)} \dot{\theta}_{(i,j)}|} \right) \right) \times 100\% \quad (5)$$

Both MAHW and HWP were computed for each motion repetition and results were used to generate boxplots for comparison (Figure 8).

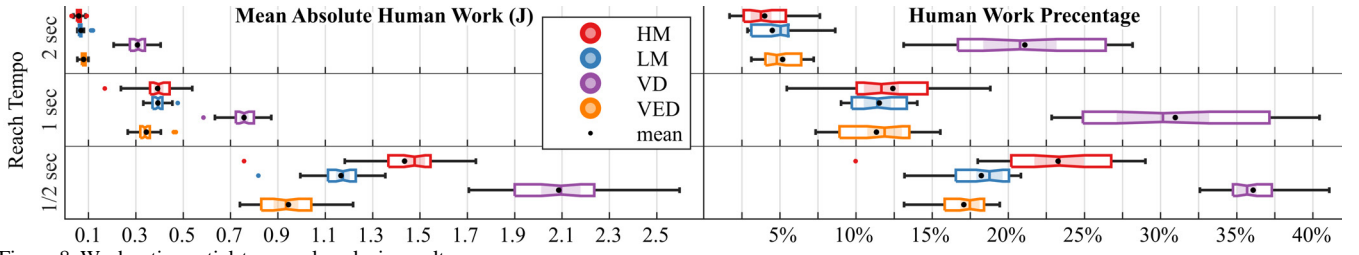


Figure 8. Work ratio spatial-temporal analysis results.

IV. DISCUSSION

A. Reduced Vibration Improved Transparency

Reduced frequency content between 5 and 10 Hz suggests that each admittance mode reduces vibration relative to the *Low-Mass* mode (Figure 6-A). The novel *Velocity-Error-Damping* performs best, achieving a 70% reduction vs *Low-Mass*. This improves the user's impression of the pHRI by rejecting disturbances that would otherwise excite the natural resonance of the combined human-robot structure. All admittance modes increased power in the 0-5 Hz band indicating improved transparency to human motion intention. Notably, Figure 6-B shows that the spatial variance of power in the 5-10 Hz band is lowest while using the *Velocity-Damping* and *Velocity-Error-Damping* modes, which indicate that the presence of damping possibly improved the consistency of control performance, and that the novel mode is at least similarly effective in this regard as a traditional damping term.

B. Naturalness of Motion

Humans naturally move in a way that minimizes sudden changes in acceleration, known as jerk [36]. Therefore, "naturalness" of recorded motions is indicated by low error to the fit minimum jerk trajectory. Results in Figure 7-C-1 suggest that the best admittance environment for promoting natural motion depends on velocity. The *Low-Mass* mode performed best in terms of average minimum-jerk trajectory error for slow (2 sec) movements. Mid-speed (1 sec) motions were most natural with the *High-Mass* mode followed by the *Velocity-Error-Damping* and *Low-Mass* modes. At higher speeds (1/2 sec) the *Velocity-Error-Damping* performed best followed by *Velocity-Damping* and *Low-Mass* modes. Interestingly, the *Low-Mass* mode was the least natural for mid-speed and fast motion, which could indicate that at higher speeds unmasked robot dynamics (e.g., vibration) may disturb the user's intended motion.

C. Tradeoff between Spatial and Temporal Accuracy

Stop-time error, (Figure 7-C-2), was consistently lowest when using the *Low-Mass* mode. For low and mid-speed motions, *Velocity-Damping* and *Velocity-Error-Damping* modes were comparable while the *High-Mass* mode caused the user to arrive late to the target resulting in significant temporal error. Motion speed also appears to correlate with temporal error. Stop accuracy, (Figure 7-C-3), was generally lowest when using the *Low-Mass* mode, but the *Velocity-Error-Damping* mode achieved the lowest error for low-speed motions. The *High-Mass* mode exhibited reduced accuracy during slow and mid-speed motions. It is possible that the presence of a non-zero impedance environment for pHRI causes the user to make a tradeoff between spatial and temporal accuracy. The virtual environment makes it

relatively easy to observe alignment error between the robot and target orientation, but timing information is more difficult to convey which may have caused the user to focus more on spatial accuracy at the cost of temporal accuracy in the presence of non-transparency.

D. Reducing User Effort

Work performed on the robot by the human was lowest for the *Velocity-Error-Damping* mode during mid-speed and fast motions; however, the *Low-Mass* and *High-Mass* modes were comparable for slow motions (Figure 8). Both higher inertia (*High-Mass* mode) and high velocity only damping (*Velocity-Damping* mode) increased the user's work share. The *High-Mass* mode caused a smaller increase than the *Velocity-Damping* mode which greatly increased user effort. While the *Low-Mass* mode creates the least impedance overall, the *High-Mass* and *Low-Mass* modes perform better for low-speed motions. This may be a result of nonlinear friction at the joints (e.g., stiction) which increases the overall damping of the system at low motions speeds.

V. CONCLUSION

While the addition of any impedance to the pHRI environment necessarily increases user effort, these results suggest that user effort can be reduced by creating an impedance environment that varies with the tracking performance of the inner-loop trajectory controller. This is demonstrated by the *Velocity-Error-Damping* mode achieving the lowest user work requirement while also decreasing vibration disturbance and improving the "naturalness" of motion trajectories.

The *Velocity-Error-Damping* mode demonstrated the best overall performance for reducing user effort and mitigating vibration disturbances. However, other modes demonstrated advantages in certain cases, e.g., the *Low-Mass* mode improved target accuracy and reduced human work at low speed. There are many additional aspects of motion that may be affected by or benefit from different pHRI environments to consider for future work. A potential tradeoff between spatial and temporal accuracy was observed, and future investigation could examine this relationship and potentially leverage high impedance force environments to magnify deficits in user path planning/execution. Future work should also consider metrics useful for post-stroke assessment such as smoothness of motion. Development of a multidomain scoring system could provide a beneficial way to compare the results of future experiments and guide the development of future devices. Additionally, results suggest that admittance controller performance depends significantly on the spatial and velocity characteristics of the desired motion, which supports the development of new methods for variable and adaptive admittance control.

ACKNOWLEDGMENT

This work is supported by NSF Award #1532239 and the Eunice Kennedy Shiver NICHD of the NIH Award #K12HD073945. The authors would also like to thank Jackson Stump, Devin Tanak, Parker Hill, Tony Branz, Melissa Bogert, and Shawn Trimble for their contributions to the design, fabrication, and CAD models used in the analysis. Special thanks to Keenan Bryan and Sandra Spearman for their help with data collection, and Jacob Friedberg for the development of the virtual environment. This paper is solely the responsibility of the authors and does not necessarily represent the official views of the NSF or the NIH.

REFERENCES

- [1] V. L. Feigin *et al.*, "Global, regional, and national burden of stroke and its risk factors, 1990–2019: a systematic analysis for the Global Burden of Disease Study 2019," *Lancet Neurol.*, vol. 20, no. 10, pp. 795–820, Oct. 2021, doi: 10.1016/S1474-4422(21)00252-0.
- [2] L. Alrabghi *et al.*, "Stroke types and management," *Int. J. Community Med. Public Health*, vol. 5, no. 9, p. 3715, Aug. 2018, doi: 10.18203/2394-6040.ijcmph20183439.
- [3] P. Langhorne, J. Bernhardt, and G. Kwakkel, "Stroke rehabilitation," *The Lancet*, vol. 377, no. 9778, pp. 1693–1702, May 2011, doi: 10.1016/S0140-6736(11)60325-5.
- [4] H. Ritchie and M. Roser, "Age Structure," *Our World Data*, Sep. 2019, Accessed: Jan. 25, 2023. [Online]. Available: <https://ourworldindata.org/age-structure>
- [5] T. Platz, L. Schmuck, S. Roschka, and J. Burrige, "Arm Rehabilitation," in *Clinical Pathways in Stroke Rehabilitation: Evidence-based Clinical Practice Recommendations*, 2021, pp. 97–121. doi: 10.1007/978-3-030-58505-1_7.
- [6] W. H. Chang and Y.-H. Kim, "Robot-assisted Therapy in Stroke Rehabilitation," *J. Stroke*, vol. 15, no. 3, pp. 174–181, Sep. 2013, doi: 10.5853/jos.2013.15.3.174.
- [7] C. M. L. Hughes, P. Tommasino, A. Budhota, and D. Campolo, "Upper Extremity Proprioception in Healthy Aging and Stroke Populations, and the Effects of Therapist- and Robot-Based Rehabilitation Therapies on Proprioceptive Function," *Front. Hum. Neurosci.*, vol. 9, 2015, Accessed: Jan. 26, 2023. [Online]. Available: <https://www.frontiersin.org/articles/10.3389/fnhum.2015.00120>
- [8] R. A. R. C. Gopura, D. S. V. Bandara, K. Kiguchi, and G. K. I. Mann, "Developments in hardware systems of active upper-limb exoskeleton robots: A review," *Robot. Auton. Syst.*, vol. 75, pp. 203–220, Jan. 2016, doi: 10.1016/j.robot.2015.10.001.
- [9] L. Santisteban, M. Térémetz, J.-P. Bleton, J.-C. Baron, M. A. Maier, and P. G. Lindberg, "Upper Limb Outcome Measures Used in Stroke Rehabilitation Studies: A Systematic Literature Review," *PLoS ONE*, vol. 11, no. 5, p. e0154792, May 2016, doi: 10.1371/journal.pone.0154792.
- [10] R. Colombo *et al.*, "Robotic techniques for upper limb evaluation and rehabilitation of stroke patients," *IEEE Trans. Neural Syst. Rehabil. Eng.*, vol. 13, no. 3, pp. 311–324, Sep. 2005, doi: 10.1109/TNSRE.2005.848352.
- [11] E. T. Wolbrecht, V. Chan, D. J. Reinkensmeyer, and J. E. Bobrow, "Optimizing Compliant, Model-Based Robotic Assistance to Promote Neurorehabilitation," *IEEE Trans. Neural Syst. Rehabil. Eng.*, vol. 16, no. 3, pp. 286–297, Jun. 2008, doi: 10.1109/TNSRE.2008.918389.
- [12] A. A. Blank, J. A. French, A. U. Pehlivan, and M. K. O'Malley, "Current Trends in Robot-Assisted Upper-Limb Stroke Rehabilitation: Promoting Patient Engagement in Therapy," *Curr. Phys. Med. Rehabil. Rep.*, vol. 2, no. 3, pp. 184–195, Sep. 2014, doi: 10.1007/s40141-014-0056-z.
- [13] T. Proietti, V. Crocher, A. Roby-Brami, and N. Jarrassé, "Upper-Limb Robotic Exoskeletons for Neurorehabilitation: A Review on Control Strategies," *IEEE Rev. Biomed. Eng.*, vol. 9, pp. 4–14, 2016, doi: 10.1109/RBME.2016.2552201.
- [14] L. Marchal-Crespo and D. J. Reinkensmeyer, "Review of control strategies for robotic movement training after neurologic injury," *J. NeuroEngineering Rehabil.*, vol. 6, no. 1, p. 20, Jun. 2009, doi: 10.1186/1743-0003-6-20.
- [15] D. Verdel, S. Bastide, N. Vignais, O. Bruneau, and B. Berret, "An Identification-Based Method Improving the Transparency of a Robotic Upper Limb Exoskeleton," *Robotica*, vol. 39, no. 9, pp. 1711–1728, Sep. 2021, doi: 10.1017/S0263574720001459.
- [16] N. Jarrassé, J. Paik, V. Pasqui, and G. Morel, "How can human motion prediction increase transparency?," in *2008 IEEE International*
- [21] "Towards Dynamic Transparency: Robust Interaction Force Tracking Using Multi-Sensory Control on an Arm Exoskeleton | IEEE Conference Publication | IEEE Xplore," <https://ieeexplore-ieee.org/uidaho.idm.oclc.org/abstract/document/9341054>.
- [22] B. Kim and A. D. Deshpande, "An upper-body rehabilitation exoskeleton Harmony with an anatomical shoulder mechanism: Design, modeling, control, and performance evaluation," *Int. J. Robot. Res.*, vol. 36, no. 4, pp. 414–435, Apr. 2017, doi: 10.1177/0278364917706743.
- [23] M. Mihelj, T. Nef, and R. Riener, "ARMin - Toward a six DoF upper limb rehabilitation robot," in *The First IEEE/RAS-EMBS International Conference on Biomedical Robotics and Biomechanics, 2006. BioRob 2006.*, Pisa, Italy: IEEE, 2006, pp. 1154–1159. doi: 10.1109/BIOROB.2006.1639248.
- [24] T. Nef, M. Guidali, V. Klamroth-Marganska, and R. Riener, "ARMin - Exoskeleton Robot for Stroke Rehabilitation," in *World Congress on Medical Physics and Biomedical Engineering, September 7 - 12, 2009, Munich, Germany*, O. Dössel and W. C. Schlegel, Eds., in IFMBE Proceedings, vol. 25/9. Berlin, Heidelberg: Springer Berlin Heidelberg, 2009, pp. 127–130. doi: 10.1007/978-3-642-03889-1_35.
- [25] A. Topini, W. Sansom, N. Secciani, L. Bartalucci, A. Ridolfi, and B. Allotta, "Variable Admittance Control of a Hand Exoskeleton for Virtual Reality-Based Rehabilitation Tasks," *Front. Neurobotics*, vol. 15, 2022, Accessed: Mar. 03, 2023. [Online]. Available: <https://www.frontiersin.org/articles/10.3389/fnbot.2021.789743>
- [26] W. Yu, J. Rosen, and X. Li, "PID admittance control for an upper limb exoskeleton," in *Proceedings of the 2011 American Control Conference*, Jun. 2011, pp. 1124–1129. doi: 10.1109/ACC.2011.5991147.
- [27] J. Bae, K. Kim, J. Huh, and D. Hong, "Variable Admittance Control With Virtual Stiffness Guidance for Human–Robot Collaboration," *IEEE Access*, vol. 8, pp. 117335–117346, 2020, doi: 10.1109/ACCESS.2020.3004872.
- [28] G. Aguirre-Ollinger, U. Nagarajan, and A. Goswami, "An admittance shaping controller for exoskeleton assistance of the lower extremities," *Auton. Robots*, vol. 40, no. 4, pp. 701–728, Apr. 2016, doi: 10.1007/s10514-015-9490-8.
- [29] J. C. Perry, R. Maura, C. K. Bitikofer, and E. T. Wolbrecht, "BLUE SABINO: Development of a Bilateral Exoskeleton Instrument for Comprehensive Upper-Extremity Neuromuscular Assessment," in *Converging Clinical and Engineering Research on Neurorehabilitation III*, L. Masia, S. Micera, M. Akay, and J. L. Pons, Eds., in Biosystems & Biobotics. Cham: Springer International Publishing, 2019, pp. 493–497. doi: 10.1007/978-3-030-01845-0_99.
- [30] A. Q. Keemink, H. van der Kooij, and A. H. Stienen, "Admittance control for physical human–robot interaction," *Int. J. Robot. Res.*, vol. 37, no. 11, pp. 1421–1444, Sep. 2018, doi: 10.1177/0278364918768950.
- [31] M. W. Spong, *Robot modeling and control* Robot modeling and control /. Hoboken, NJ : John Wiley & Sons, 2006.
- [32] R. M. Murray, Z. Li, and S. S. Sastry, *A mathematical introduction to robotic manipulation*. CRC press, 2017.
- [33] J. C. Perry, J. Rosen, and S. Burns, "Upper-Limb Powered Exoskeleton Design," *IEEE/ASME Trans. Mechatron.*, vol. 12, no. 4, pp. 408–417, Aug. 2007, doi: 10.1109/TMECH.2007.901934.
- [34] R. Maura, "Development of a Safe Force-Based Controller to Obtain Reliable Stroke Metrics from an Exoskeleton," UI, 2023.
- [35] S. A. Wall and W. Harwin, "A high bandwidth interface for haptic human computer interaction," *Mechatronics*, vol. 11, no. 4, pp. 371–387, Jun. 2001, doi: 10.1016/S0957-4158(00)00024-6.
- [36] N. Hogan, "An organizing principle for a class of voluntary movements," *J. Neurosci.*, vol. 4, no. 11, pp. 2745–2754, Nov. 1984, doi: 10.1523/JNEUROSCI.04-11-02745.1984.